ACS APPLIED MATERIALS & INTERFACES

www.acsami.org

Research Article

Enhanced Electron Transfer Efficiency of Fructose Dehydrogenase onto Roll-to-Roll Thermal Stamped Laser-Patterned Reduced Graphene Oxide Films

Davide Paolini, Flavio Della Pelle,* Annalisa Scroccarello, Filippo Silveri, Paolo Bollella, Giovanni Ferraro, Eole Fukawa, Yohei Suzuki, Keisei Sowa, Luisa Torsi, and Dario Compagnone*

Cite This: *ACS Appl. Mater. Interfaces* 2024, 16, 22443−22454

Read Online

ACCESS | Metrics & More | Article Recommendations | Supporting Information

ABSTRACT: Herein, a strategy to stamp laser-produced reduced graphene oxide (rGO) onto flexible polymers using only office-grade tools, namely, roll-to-roll thermal stamping, is proposed, proving for the first time its effectiveness for direct bioelectrocatalysis. This straightforward, scalable, and low-cost approach allows us to overcome the limits of the integration of laser-induced rGO-films in bioanalytical devices. Laser-produced rGO has been thermally stamped (TS) onto different polymeric substrates (PET, PVC, and EVA) using a simple roll-laminator; the obtained TS-rGO films have been compared with the native rGO (untransferred) via morphochemical and electrochemical characterization. Particularly, the direct electron transfer (DET) reaction between fructose dehydrogenase (FDH) and TS-rGO transducers has been investigated, with respect to the influence of the amount of enzyme on the catalytic process. Remarkable differences have been observed among TS-rGO transducers; PET proved to be the elective substrate to support the transfer of the laser-induced rGO, allowing the preservation of the morphochemical features of the native material and returning a reduced capacitive current. Noteworthily, TS-rGOs ensure superior electrocatalysis using a very low amount of FDH units (15 mU). Eventually, TS-rGO-based third-generation complete enzymatic biosensors were fabricated via low-cost benchtop technologies. TS-rGO$_{PET}$ exhibited bioanalytical performances superior to the native rGO, allowing a sensitive (0.0289 μA cm^{-2} μM^{-1}) and reproducible (RSD = 3%, n = 3) D-fructose determination at the nanomolar level (LOD = 0.2 μM). TS-rGO exploitability as a point-of-need device was proved via the monitoring of D-fructose during banana (*Musa acuminata*) postharvest ripening, returning accurate (recoveries 110−90%; relative error −13/+1%) and reproducible (RSD ≤ 7%; n = 3) data.

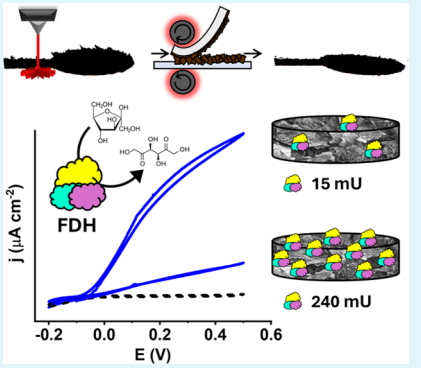

KEYWORDS: *reduced graphene oxide, CO^2-laser, biocatalysis, flexible biosensors, nanomaterial conductive films, electrochemical biosensors*

1. INTRODUCTION

Over the last decades, carbonaceous materials greatly affected applied nanotechnology and among them, graphene is still considered the 'gold nanomaterial' for bioelectronics.[1] Graphene is a two-dimensional nanomaterial characterized by a wide surface area and unique electrical and mechanical features, which make it attractive for advanced electronics, including capacitors, transistors, and sensing devices.[2,3] Pure graphene presents some limitations, in particular regarding synthesis, poor water-solubility, and stability; this makes it complex to both handle and integrate into lab-made devices. Therefore, graphene derivatives have gained attention; among others, graphene oxide (GO) is particularly appealing because of its water-dispersibility, stability, and ease of manipulation.[4] GO is produced through oxidation treatments starting from graphite, resulting in a graphene surface chemistry rich in oxygen moieties (hydroxyl groups, carboxyl groups, etc.); this surface chemistry provides reactive domains for chemical modification/functionalization and results useful for band gap-based electronics.[5,6] On the other hand, GO's low electrical conductivity imparts an insulating or semiconductive behavior to this material, which represents a strong limit for (bio)electrochemical applications based on electron transfer reactions.

Several efforts have been devoted to converting GO into its conductive and electrochemically active counterpart, i.e., reduced graphene oxide (rGO); among the various proposed approaches chemical reduction, thermal annealing, and laser-assisted photothermal reduction have been reported.[7,8] Chemical reduction involves the use of different chemicals as

Received: February 28, 2024
Revised: April 6, 2024
Accepted: April 9, 2024
Published: April 17, 2024

https://doi.org/10.1021/acsami.4c03339
ACS Appl. Mater. Interfaces 2024, 16, 22443−22454

Scheme 1. Sketch of the TS-rGO Sensor Manufacturing[a]

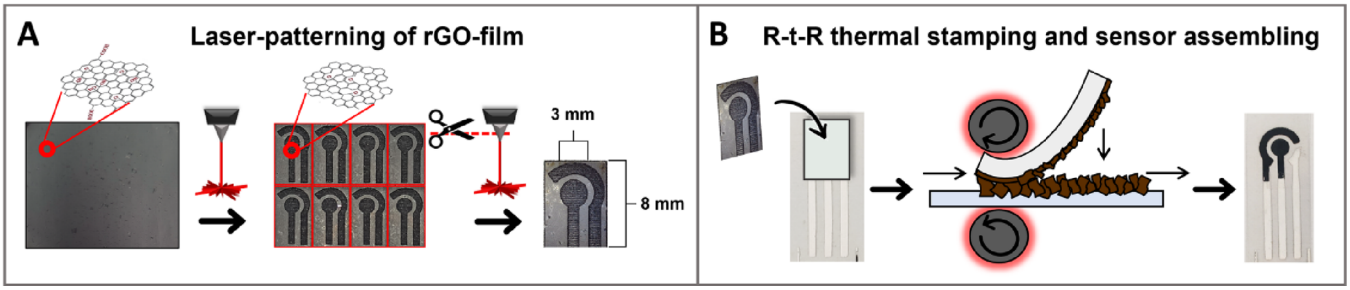

[a](A) Serial laser-induced formation of rGO-based working and counter electrodes, starting from GO film. (B) Roll-to-roll thermal stamping of rGO working and counter electrodes by roll-to-roll thermal laminator onto a substrate enclosing the complementary contacts.

hydrazine, sodium borohydride, and ascorbic acid.[9] Although this method can produce rGO in solution, the formation of other functional groups on the surface of the material may occur due to the use of reducing agents.[8] In thermal annealing, GO is reduced to rGO via high temperatures, causing the production CO and CO_2,[10] which may cause the elimination of carbon atoms from the GO structure. This triggers graphene sheets cracking into smaller fragments bringing additional distortion to the sp^2 carbon plane.[11] For sensor fabrication, both methods exhibit the limit of forming thin conductive rGO films onto flexible polymeric supports.

Laser photothermal reduction represents an effective approach to form rGO-nanostructured conductive films, using a CO_2 laser plotter only.[12] In this approach, GO film is irradiated with a laser beam and instantly converted in situ to rGO. Kaner et al.[13] proposed this approach for the first time, in this case, a standard LightScribe DVD was employed to drive the direct laser reduction of graphite oxide to graphene, proving that the produced films possess mechanical and electrical features particularly useful for electrochemical capacitors development. The same group proposed the modification of different solid substrates with the same material, demonstrating for the first time application in gas sensing.[14] No doubt, laser-patterning is a straightforward approach to form conductive rGO patterns with micrometric resolution, particularly prone to microelectronic and (bio)sensing platform development.[6,15]

In electroanalytical chemistry, the integration of rGO conductive films onto polymeric flexible substrates is still an open issue. Indeed, the transfer of the nanomaterial on the polymer is crucial to define the structural and electrochemical characteristics of the resulting film. Beyond classic methods, which require expensive and complex equipment, not applicable to all substrates, often rGO transferring is achieved by using solvents and/or chemical treatments devoted to enhance its adhesion.[7] Another approach relies on press-transferring, which demonstrated remarkable efficiency for rGO and other carbonaceous nanomaterials.[16,17] Nevertheless, this strategy requires the application of high pressures that can damage the substrates and trigger the restacking of graphene with a loss of performance. An easy emerging approach is represented by xurography, which exploits thermal lamination to transfer films of nanomaterials onto thermal-adhesive substrates.[18] Despite this approach allowing assembly of electrochemical sensors,[19,20] it has never been attempted for laser-produced materials to the best of our knowledge.

Direct electron transfer (DET)-type bioelectrocatalysis is one of the most challenging subjects in modern bioelectrochemistry. This approach has been widely explored to build up biofuel cells and third generation enzymatic sensors. To improve DET-type bioelectrocatalysis, electrode/transducer nanostructuration is a key aspect that needs to be carefully tuned for each enzyme.[21] Among redox enzymes, fructose dehydrogenase (FDH) from *Gluconobacter japonicus* has been employed for D-fructose determination; FDH is a membrane-bound protein characterized by three subunits, which can communicate directly with the electrode/transducer if properly modified/nanostructured.[22,23] Among several electroanalytical applications, rGO-based sensors, mainly commercially available electrodes modified with rGO, have been employed as platforms for proteins and redox enzymes.[24] To the best of our knowledge, laser-produced rGO has not been studied for DET-based electronics, despite its nanostructure and remarkable charge-transfer ability, which may suggest huge potential for electrocatalysis.

In this work, laser-produced rGO nanostructured films were stamped onto different flexible plastic substrates through a xurography-based approach named 'roll-to-roll thermal stamping' (R-t-R TS). TS-rGO films were carefully morphochemically and electrochemically characterized, revealing how the stamping changes the rGO native nature and the employed support affects the film features. Afterward, particular efforts were devoted to the investigation of TS-rGO sensors' DET-ability using FDH as a model enzyme. TS-rGO platforms ensured high and reproducible electroanalytical performances using a very low amount of FDH units. Among substrates, PET has emerged as the elective substrate to fabricate TS-rGO biosensors. Finally, the TS-rGO_{PET} biosensors were employed to monitor D-fructose evolution in banana fruits (*Musa acuminata*) during postharvest ripening carried out in different conditions.

2. MATERIALS AND METHODS

2.1. Chemicals and Materials. Sodium acetate, potassium chloride, potassium ferrocyanide, potassium ferricyanide, ruthenium hexamine, D-fructose, ascorbic acid, citric acid, glucose, sucrose, maltose, mannitol, L-tryptophan, L-tyrosine, L-lysine, L-cysteine, NaCl, $CaCl_2$, $MgCl_2$, K_2HPO_4, KOH, and KCl were purchased from Sigma-Aldrich (St Louis, MO, USA). Graphene oxide (GO) stock dispersion (10 mg mL^{-1}) was obtained from Angstrom Materials (Dayton, Ohio, USA). Recombinant fructose dehydrogenase (FDH, native type EC 1.1.99.11) from *Gluconobacter japonicus* NBRC 3260 (40 U mg^{-1}) was expressed and purified as reported previously.[25] Polyvinylidene fluoride (PVDF) membrane (0.1 μm of pore size, 47 mm of diameter) was purchased from Millipore (Massachusetts, USA). Polyethylene terephthalate sheets (PET) (0.2 mm), polyethylene terephthalate-ethylene vinyl acetate laminating sheets (EVA) (0.2 mm), and smooth polyvinyl chloride sheets (PVC) (0.2 mm) were purchased from Fellowes (Itasca, Illinois, USA). Silver paste (C2100203D2) was purchased from Gwent group/Sun Chemical (Pontypool, U.K.) and

https://doi.org/10.1021/acsami.4c03339
ACS Appl. Mater. Interfaces 2024, 16, 22443−22454

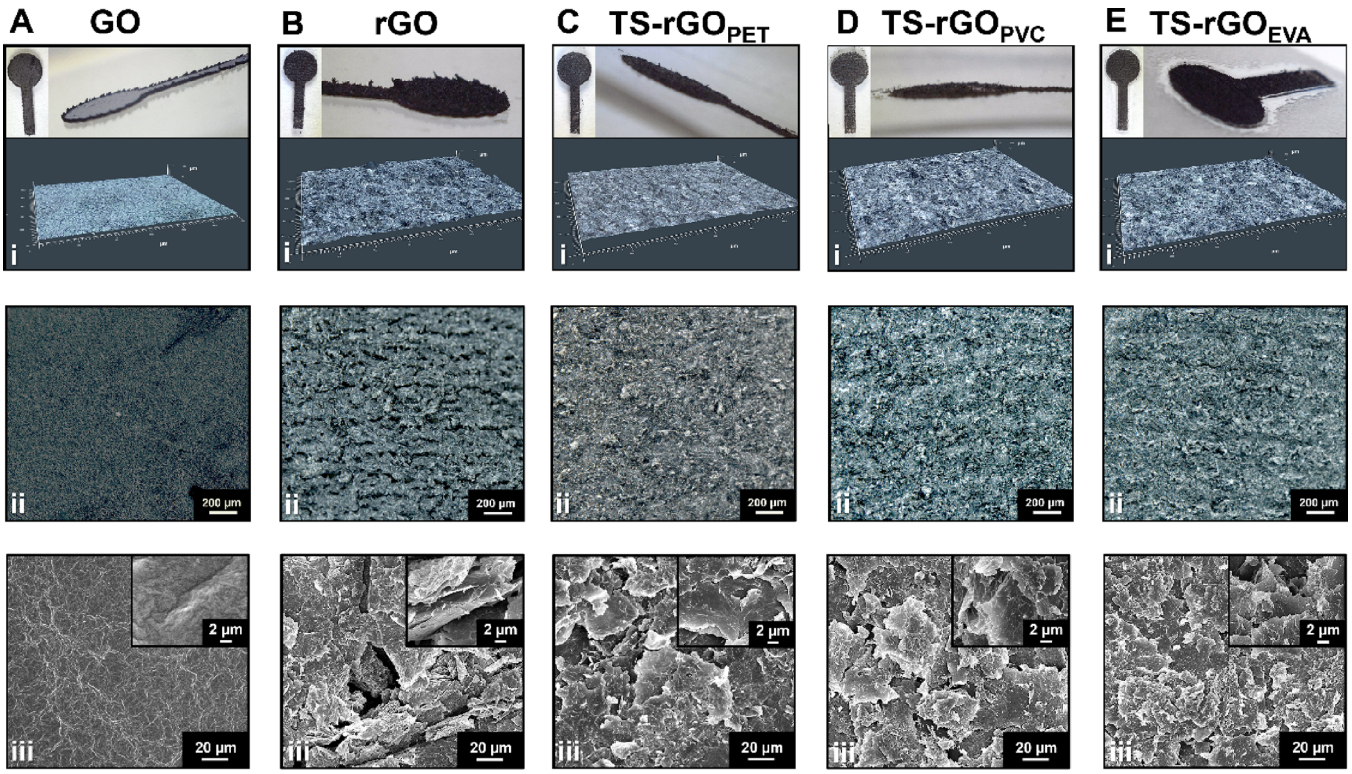

Figure 1. Morphological characterization of (A) GO film, (B) rGO film, (C) TS-rGO$_{PET}$, (D) TS-rGO$_{PVC}$, and (E) TS-rGO$_{EVA}$ performed with (i) optical and reflected light microscopy, (ii) stereo microscopy, and (iii) scanning electron microscopy with In-lens detector magnification 500× (insets magnification at 5k×).

used to print contacts and reference electrodes; dielectric paste (Sylgard 184) was purchased from VWR International srl (Milano, Italy) and employed for electrode contacts insulation. Milli-Q grade water (18.2 MΩ cm, Millipore, Bedford, MA, USA) was used to prepare all solutions.

2.2. Roll-to-Roll Thermal Stamping of Laser-Induced rGO and Sensor Assembling. A Rayjet50 laser machine from Trotec (Wels, Austria) equipped with a CO_2 laser beam (10.6 μm, 30 Wcw, laser spot of 0.04 mm) was employed to convert GO in rGO; rGO-working (W) and counter (C) electrode design was defined using Adobe Illustrator 2020 software. A Silhouette Cameo craft cutter 4 (Silhouette America, Lindon, USA) equipped with Silhouette 4.4 software was employed to design the stencil masks used to print the silver-ink contacts on the sensor base; in brief, silver-ink was spread with a squeegee, the stencil mask was removed, and the printed contacts cured (60 °C, 30 min). Sensors were assembled on different substrates (i.e., PET, PVC, and EVA) to form three complete electrodes containing electrochemical cells with the laser-induced rGO used as W and C electrodes. A graphical sketch of the sensors' fabrication, with pictures of the main components, is reported in Scheme 1, while Video S1 records the R-t-R TS process.

Scheme1A, laser-patterning of rGO-film: commercial GO stock dispersion (10 mg mL^{-1}) was diluted in 5 mL of water to reach the final concentration of 1.25 mg mL^{-1}; GO dispersion was vortexed for 30 s, filtered on a PVDF membrane, and dried at room temperature. The GO amount used to form the film was selected according to our group's previous studies.[26]. The GO-film was treated with the CO_2 laser under a 7.4 cm focusing lens, using the engraving mode (laser power 8 W; speed 100 m s^{-1}); a key-lock-like pattern obtained using Corel Draw software was employed to define W (Ø = 3 mm) and C electrodes design. Single W and C electrode couples were cut out on rectangles (8 mm × 6 mm) through the CO_2 laser using the cutting mode (power 6 W and speed 3 m s^{-1}).

Scheme1B, roll-to-roll thermal stamping and sensor assembling: W and C rGO electrodes were aligned above the sensor base according to the electrical contact complementary pattern, sandwiched between two sheets of office paper (to maintain alignment), and the rGO stamping was achieved by passing through a roll-to-roll thermal laminator T 72 ± 1 °C (Pavo 8038718, Unbekannt, Germany). Eventually, the PVDF filter was removed, and the electrode contacts were insulated using the dielectric paste.

According to the substrate employed, the thermally stamped (TS) sensors were named TS-rGO$_{PET}$, TS-rGO$_{PVC}$, and TS-rGO$_{EVA}$.

To investigate the features of native rGO (before R-t-R stamping), an additional sensor was manufactured; in this case, the rGO-film onto the PVDF membrane was cut out, using the CO_2 laser, following the W electrode borders pattern. Afterward, the electrode was lain onto a preheated thermo adhesive substrate. In this case, silver contacts were manually printed and cured (60 °C, 30 min), and electrode contacts were insulated using the dielectric paste; this sensor was named 'rGO'.

2.3. Characterization of the Nanostructured Films. Macroscopic pictures of the electrodes were collected through a Digital Microscope ADSM302 (Andonstar, China) and ZEISS Axio Zoom.V16 microscope (Zeiss Co., Oberkrochen, Germany). Profilometric pictures were collected with an Olympus BH-2 reflected light microscope equipped with a Leica EC3 Camera detector (Olympus Corporation, Bartlett, TN).

Scanning electron microscopy (SEM) micrographs were acquired with a GeminiSEM 500 instrument (Zeiss Co., Oberkrochen, Germany) using an InLens detector, working at a distance of 3 mm with an acceleration potential of 3 kV; micrographs were acquired on Cr plasma-coated samples. The morphochemical features were investigated via Raman spectroscopy; the spectra were acquired using a Renishaw InViaReflex confocal Raman microscope with a Leica DM microscope, focusing the laser with a 50LX objective on the sample (NA 0.50, WD 8.20 mm). A 532 nm laser line (diode-type, Renishaw 80 mW 532 nm laser, 1800 l mm^{-1} grating) was employed. The data were processed using Renishaw WiRE 3.2 software, acquiring the spectra in the range between 200 and 5498 cm^{-1} using the static mode, with a spectral resolution of 0.88 cm^{-1}.

Electrochemical measures were performed with a Palmsens 4 Potentiostat/Galvanostat/Impedance Analyzer (Palm Instruments

https://doi.org/10.1021/acsami.4c03339
ACS Appl. Mater. Interfaces 2024, 16, 22443−22454

BV, Houten, Netherlands) managed by PS trace software. To compare the electrochemical features of the sensors, the respective working electrode was connected with an external counter (Pt wire) and reference (Ag/AgCl and 3 M KCl) electrode. Cyclic voltammetry (CV) was performed at 10 mV s^{-1} using 5 mM $[Fe(CN)_6]^{3-/4-}$ and 5 mM $[Ru(NH_3)_6]^{3+/2+}$ both containing 0.1 M KCl. Electrochemical impedance spectroscopy (EIS) was performed using 5 mM $[Fe(CN)_6]^{3-/4-}$ containing 0.1 M KCl, setting the potential at the open circuit, using a sinusoidal wave with a 5 mV amplitude, scanning the frequencies between 10^{-1} and 10^5 Hz. Double layer capacitance (C_S) was investigated via CVs at increasing scan rates (from 0.04 to 0.2 V s^{-1}) in KOH 0.1 M, operating in a nonfaradaic region. Graphite screen-printed electrodes (SPE) used as a comparison were purchased from Eco BioServices (Florence, Italy).

2.4. Bioelectrocatalytic Studies. Bioelectrocatalytic features were investigated by drop-casting different amounts of a 40 U mg^{-1} FDH suspension onto the sensors' working electrode surfaces (Section 3.2); after the deposition, the electrodes were left 45 min in the dark. Direct electron-transfer (DET) reaction was evaluated by performing the measurements in an electrochemical cell with external counter and reference electrodes (details in Section 2.3). CVs at 5 mV s^{-1} in 50 mM acetate buffer solution (pH 4.5) containing 0.1 M KCl were carried out in the absence and presence of 10 mM D-fructose. Amperometry in acetate buffer (pH 4.5) containing 0.1 KCl was employed for D-fructose biosensing; in this case, the complete three-electrode biosensors working at a potential of +0.15 V (vs Ag) were modified with 15 and 240 mU of FDH.

2.5. Proof of Applicability. The analytical exploitability of TS-rGO biosensors was proved by monitoring the D-fructose evolution during bananas (*Musa acuminata*) postharvest ripening. Bananas belonging to the same lot, collected at the same time, were purchased from local food markets, and stored at room temperature in the dark under two different conditions: (i) closed in a sealed bag and (ii) kept in open air. D-Fructose monitoring was conducted for 22 days, sampling every 3/2 days; for each sampling, three different bananas were used. Before the analysis, the bananas were peeled off and homogenized.[27] Then, 5 g of banana pulp was placed in 20 mL of Milli-Q water, vortexed (30 s) and centrifuged at 10000*g* for 10 min to remove the solid components. Eventually, banana samples were filtered by a syringe filter (VWR, 0.45 μm, nylon) and rapidly analyzed. Samples were thus diluted in acetate buffer and D-fructose was measured via amperometry (+ 0.15 V vs Ag) using the TS-rGO_{PET} biosensor.

To compare the data obtained with the proposed biosensor, banana samples were analyzed also using a commercial enzymatic colorimetric kit for D-fructose quantification following the supplier procedure (MAK265; Sigma-Aldrich, St Louis MO, USA).

3. RESULTS AND DISCUSSION

3.1. R-t-R Thermal-Stamped rGO: Concept and Physicochemical Features. Reduced graphene oxide (rGO) film production and patterning were carried out via a photothermal approach through a laser-plotter, starting from graphene oxide (GO); then, the rGO-film was transferred on PET (TS-rGO_{PET}), PVC (TS-rGO_{PVC}), and EVA (TS-rGO_{EVA}) substrates via R-t-R thermal transfer (TS). Scheme 1 schematically reports the transferring process and the TS-rGO sensor fabrication, while Video S1 records the R-t-R TS process. Detailed rGO-film production and sensor fabrication are reported in Section 2.2. To understand the stamping effect on the laser-produced conductive film, the native untransfered rGO-film was also studied (later referred to as 'rGO').

Figure 1 reports the morphological characterization of the GO, rGO, TS-rGO_{PET}, TS-rGO_{PVC}, and TS-rGO_{EVA} surfaces.

GO and rGO films were initially characterized to confirm the photoreduction process. Figures 1A(i-ii),1B(i-ii) confirms the presence of a laser-driven photoreduction process. Notably, the untreated GO-film appeared flat with a homogeneous and regular profile while rGO-film showed the typical 3D edgy profile characterized by an out-of-the-plane highly wrinkled surface, attributable to laser-produced rGO.[28] This structural change was further evidenced by the profilometric pictures, where rGO exhibited darker and brighter areas due to cracks/furrows and exploded/out-of-plane flakes, respectively. SEM micrographs confirmed the laser-induced variations, with GO film (Figure 1Aiii) having a uniform surface due to stacked GO sheets, and rGO film (Figure 1Biii) with an exfoliated-like and porous network, composed of overlapped flakes interposed at deep crack/grooves. This suggests a 3D configuration typical of graphenic-based materials obtained via laser-photothermal reduction.[28]

The TS-rGO surfaces were then investigated to understand their morphological variation and the ability of the different substrates (i.e., PET, PVC, and EVA) to support and accommodate the rGO films. Figure 1C−Ei highlights the similarities between rGO films and native rGO at the macroscopic level. For all the substrates, the film is characterized by a not-so-prominent out-of-the-plane thickness, attributable to the R-t-R thermal-stamping process, where only part of the material is transferred, and the same undergoes a tearing effect during PVDF filter removal. Optical reflection microscopy (Figures 1C−Eii) confirms the changes in the material morphology concerning the native rGO. Figures 1C−Eiii reports TS-rGO SEM micrographs showing homogeneous nanostructured surfaces characterized by ordered flakes without macro pits or cracks where the hosting substrate is exposed. This and the conductivity of all the TS-rGO films prove the effectiveness of the transferring process. All the TS-rGO films appear more flat compared to rGO; among TS-rGO films, TS-rGO_{EVA} (Figure 1Eiii) appeared more uneven with smaller overlapped flakes. This effect could be attributed to the tearing effect related to EVA termoadhesivity. On the other hand, TS-rGO_{PET} (Figure 1Ciii) and TS-rGO_{PVC} (Figure 1Diii) show a similar structure with overlapped flakes with micrometric lateral dimensions mostly arranged horizontally.

The physicochemical features of all the systems were further investigated through Raman spectroscopy. Figure 2 reports the

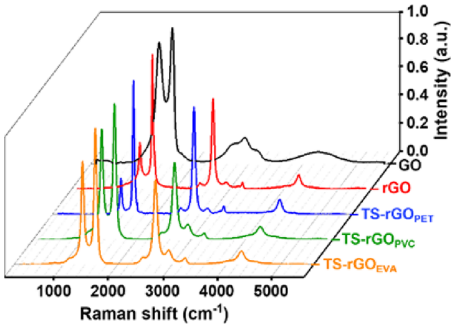

Figure 2. Raman spectra of GO film (black line), rGO film (red line), TS-rGO_{PET} (blue line), TS-rGO_{PVC} (green line), and TS-rGO_{EVA} (orange line).

Raman spectra; the D (~1350 cm^{-1}) and G (~1580 cm^{-1}) bands, characteristics of graphene, are present in all of the substrates; a well-defined 2D band (~2700 cm^{-1}) appears only after the laser treatment.

According to the literature, the D band indicates the degree of defects since it is assigned to the primary in-plane vibrations of the sp^3 carbon, while the G band is associated with the stretching

https://doi.org/10.1021/acsami.4c03339
ACS Appl. Mater. Interfaces 2024, 16, 22443−22454

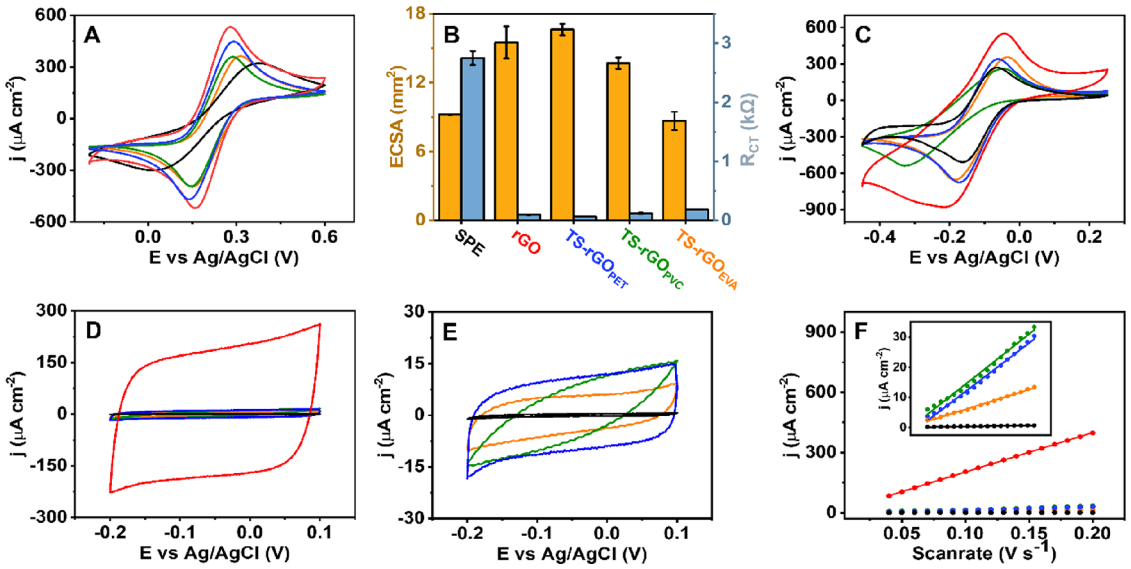

Figure 3. Electrochemical characterization. Legend: SPE (black), rGO-film (red), TS-rGO$_{PET}$ (blue), TS-rGO$_{PVC}$ (green), and TS-rGO$_{EVA}$ (orange). (A) Cyclic voltammograms for 5 mM $[Fe(CN)_6]^{3-/4-}$ in 0.1 M KCl at 10 mV s^{-1}. (B) Double columns plot reporting the electrochemical active surface area (yellow bars) and charge transfer resistance (cyan bars) extrapolated values. (C) Cyclic voltammograms for 5 mM $[Ru(NH_3)_6]^{3+/2+}$ in 0.1 M KCl at 10 mV s^{-1}. (D) Cyclic voltammograms for all the films in the nonfaradic region obtained in 0.1 M KOH at 0.1 V s^{-1}. (E) Cyclic voltammograms for TS-rGO$_{PET}$, TS-rGO$_{PVC}$, TS-rGO$_{EVA}$, and SPE in the nonfaradaic region obtained in 0.1 M KOH at 0.1 V s^{-1}. (F) Linear relationship between the density nonfaradaic current and scan rate for double layer capacitance extrapolation; measurement performed in 0.1 M KOH at scan rate between 0.04 and 0.2 V s^{-1}. The inset reports a magnification at which the rGO-film is excluded.

of sp^2 atoms. The 2D band is ascribed to the two-dimensional plane rearrangement of graphene and is associated with the exfoliation degree since it is related to the number of graphene layers.[29−31] A marked decrease of the I_D/I_G ratio is observed after the laser processing, from 0.89 ± 0.03 of GO (black line) to 0.23 ± 0.01 of rGO (red line); all the extrapolated I_D/I_G ratios are expressed as average values of three different transducers of the same type. This result proves the decrease of sp^3 carbon and the re-establishment of the sp^2 domains. This aspect confirms the effectiveness of the laser treatment, which induces the reduction of the oxygen-containing groups of GO by harsh expulsion, which leads to the formation of highly exfoliated rGO. The latter phenomenon is confirmed by the appearance of a predominant and sharp 2D peak.[28]

Noteworthily, the I_D/I_G ratio appears different among TS-rGOs. TS-rGO$_{PET}$ (blue line) is the most similar to native rGO as revealed by the similar I_D/I_G ratio (0.27 ± 0.02), suggesting the retention of native rGO features after film stamping. This is further confirmed by the high intensity of the 2D band obtained for TS-rGO$_{PET}$ comparable to that of native rGO. TS-rGO$_{PVC}$ (0.81 ± 0.03, green line) and TS-rGO$_{EVA}$ (0.75 ± 0.04, yellow line) showed higher I_D/I_G ratio values, which were more similar to GO. The latter observation may indicate that rGO flake restacking is due to the thermal-stamping or loss of native conformation of rGO obtained with the laser. The presence of more physicochemical defects in both TS-rGO$_{PVC}$ and TS-rGO$_{EVA}$ is further confirmed by more pronounced G+D and 2G peaks (~2876−3310 cm^{-1}).[6]

The observed differences among all the investigated samples can be attributed to the different chemistry of the plastic material used as a support for rGO, mainly their different glass transition temperatures (T_{gEVA} ~ −30 °C < T_{gPET} ~ 71 °C < T_{gPVC} ~ 95 °C) and melting temperatures (T_{mEVA} 70−90 °C < T_{mPVC} 100−260 °C < T_{mPET} 240−270 °C), affecting the R-t-R thermal transferring and rGO-film deposition. To preserve the native rGO chemistry, it is necessary to reach the Tg without exceeding the T_m; this occurs for PET.

The electrochemical features of all the prepared surfaces were then investigated using an inner- and outer-sphere redox probe, i.e., $[Fe(CN)_6]^{3-/4-}$ and $[Ru(NH_3)_6]^{3+/2+}$, respectively. The GO film was not considered because it is not conductive. Electrochemical studies were also compared to a commercial graphite screen-printed electrode (SPE). The electrochemical parameters together with the respective standard deviations obtained from measures performed in triplicate are listed in Tables S1 and S2.

Figure 3A shows cyclic voltammograms obtained in $[Fe(CN)_6]^{3-/4-}$: all the rGO-based films showed a clear improvement of the electrochemical features compared to SPE (j_{pa} = 270 ± 17 μA cm^{-2}; ΔE = 327 ± 12 mV; black curve) as demonstrated by the significant peak intensity increase (j_{pa}) and peak-to-peak separation (ΔE) decrease.

Noteworthily, the best-performing films appear to be rGO (j_{pa} = 545 ± 26 μA cm^{-2}; ΔE = 127 ± 12 mV; red curve) and TS-rGO$_{PET}$ (j_{pa} = 587 ± 19 μA cm^{-2}; ΔE = 140 ± 8 mV; blue curve) followed by TS-rGO$_{PVC}$ (green curve) and TS-rGO$_{EVA}$ (orange curve). This trend is confirmed by the electrochemical active surface area (ECSA) extrapolated according to Randles−Sevcik's theory for quasi-reversible systems;[32] the ECSA was similar for the native rGO and TS-rGOs (Figure 3B, yellow bars), despite the transferring process. In particular, TS-rGO$_{PET}$ resulted in the largest ECSA value (16.6 ± 0.5 mm^2) slightly higher than the native rGO (15.5 ± 1.4 mm^2). Thus, the film after stamping (TS-rGOs) preserves the rGO features and shows a decrease in the capacitive current (this important issue will be further discussed in this section).

The electron transfer features were further explored by studying the charge transfer resistance (R_{CT}) via EIS and extrapolating the heterogeneous electron transfer constant (k^0) according to Nicholson's method for quasi-reversible sys-

https://doi.org/10.1021/acsami.4c03339
ACS Appl. Mater. Interfaces 2024, 16, 22443−22454

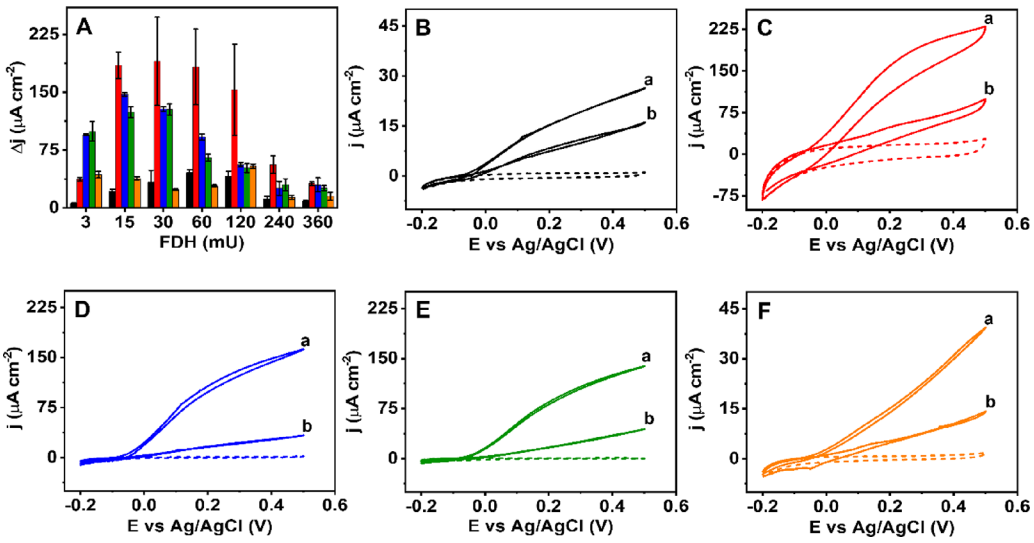

Figure 4. DET investigation. Legend: SPE (black), rGO (red), TS-rGO$_{PET}$ (blue), TS-rGO$_{PVC}$ (green), and TS-rGO$_{EVA}$ (orange). (A) Catalytic density current (Δj) recorded at +0.4 V (vs Ag/AgCl), obtained for the whole set of films modified with different units of FDH; FDH units studied are reported in the figure. Data are extrapolated from CVs performed in 10 mM D-fructose in acetate buffer, and Δ*j* has been calculated by subtracting the capacitive density current (blank) at the faradaic catalytic density current. (B–F) Cyclic voltammograms obtained in acetate buffer, before (dashed curves) and after the addition of 10 mM D-fructose (full curves); scan rate of 5 mV s^{-1}. CVs were performed for SPE (B), rGO (C), TS-rGO$_{PET}$ (D), TS-rGO$_{PVC}$ (E), and TS-rGO$_{EVA}$ (F) modified with 15 mU (a) and 240 mU (b) of FDH; the measure in the absence of D-fructose is referred to as FDH 15 mU.

tems.[33,34] Figure S1 shows the Nyquist's plots obtained for the different films, while in Figure 3B (cyan bars), the differences obtained among the R_{CT} values are visible; the R_{CT} values were extrapolated by fitting the EIS spectra with the Randles equivalent circuit (Figure S2A). The SPE is characterized by a wide semicircle that results in an R_{CT} of 2751 ± 4 Ω, native rGO resulted in a dramatically lower R_{CT} (95 ± 2 Ω), and slightly higher values were obtained for TS-rGO$_{EVA}$ (183 ± 2 Ω) and TS-rGO$_{PVC}$ (119 ± 9 Ω); TS-rGO$_{PET}$ showed the smallest R_{CT} value (65 ± 5 Ω), proving the lower charge transfer resistance.

The heterogeneous electron transfer returned a similar behavior, where the rGO-based films possess k^0 values significantly higher than SPE (0.5×10^{-3} cm s^{-1}). Similar k^0 values were obtained for the native rGO-film and TS-rGOs (k^0 between 3.0×10^{-3} and 3.8×10^{-3} cm s^{-1}), except for TS-RGO$_{EVA}$, which showed a slightly lower value (2.4×10^{-3} cm s^{-1}). Overall, these data demonstrate how the R-t-R thermal stamping process did not compromise the electron transfer ability of native rGO.

Figure 3C reports the $[Ru(NH_3)_6]^{3+/2+}$ cyclic voltammograms, and Table S2 lists the relative electrochemical parameters extrapolated. This outer-sphere redox probe is mainly influenced by the density of electronic states and independent of the micro/nanostructure of the film material,[35] bringing out differences among rGO-based films. In particular, the native rGO voltammogram shows a not very well-defined shape characterized by a significantly lower j_{pa} (309 ± 39 μA cm^{-2}) compared to TS-rGO$_{PET}$ (j_{pa} = 609 ± 17 μA cm^{-2}); moreover, TS-rGO$_{PET}$ exhibited a slightly lower Δ*E* (129 ± 21 mV) compared to rGO (145 ± 11 mV), indicating faster electron transfer mechanism. TS-rGO$_{PVC}$ demonstrates the worst electron-transfer capabilities toward this probe, while TS-rGO$_{EVA}$ shows an intermediate behavior. These data reveal that the R-t-R transfer and the hosting substrate employed play key roles in the electrochemical properties of the obtained graphene films.

To better investigate the effect of the R-t-R stamping on the electric double layer, the capacitance (C_S) was also evaluated, performing CV measures in the nonfaradaic region at increasing scan rates, using KOH as support electrolyte. Contrary to the ECSA trend, a dramatic difference between C_S values for the native rGO and TS-rGOs was registered, as shown in Figure 3D. Figure 3E reports that the CVs of all the films excluded the native rGO. Figure 3F shows the outcome of the double-layer capacitance investigation: C_S has been extrapolated from the slope of the linear relationship between the density of nonfaradaic current (j, μA cm^{-2}) and the scan rate (ν, V s^{-1}) described by the equation $j = C_S\nu$.[36] Figure S3 depicts the complete voltammetry scan rate study for native rGO and TS-rGO$_{PET}$. Native rGO-film demonstrates the highest C_S (1.9612 μF cm^{-2}), an order of magnitude greater compared to TS-rGOs. Among TS-rGOs, TS-rGO$_{PET}$ (0.1599 μF cm^{-2}) and TS-rGO$_{PVC}$ (0.1613 μF cm^{-2}) showed higher C_S than the other film (TS-rGO$_{EVA}$: 0.0671 μF cm^{-2}; SPE: 0.0035 μF cm^{-2}). Interestingly, the C_S trend does not agree perfectly with the redox investigation previously discussed; indeed, despite voltammograms with different shapes (Figure 3E), TS-rGO$_{PET}$ and TS-rGO$_{PVC}$ exhibited similar C_S values, both higher than those of TS-rGO$_{EVA}$.

The prominent 3D-wrinkled structure of native rGO confers to the film a tremendous capacitance that negatively influences the faradaic/capacitive current ratio for redox probes analysis. After R-t-R thermal stamping, capacitance dramatically decreases, not always resulting in an improvement of the electrochemical features. Despite the slight difference in the morphology among TS-rGOs, significantly different electrochemical behaviors were registered.

Taking a closer examination of the literature, the proposed strategy, despite the need for more than a single step for material preparation and transferring, returns electrochemical features comparable to laser-induced graphene films. Table S3 resumes the main features, electrochemical figures of merit, and

https://doi.org/10.1021/acsami.4c03339
ACS Appl. Mater. Interfaces 2024, 16, 22443−22454

applications of laser-induced graphene based on the transferring strategies reported in the literature. Most of the strategies use hydraulic presses and/or thermoheated hydraulic presses to transfer the films. In our case, an office tool is used, the roll-to-roll laminator (cost lower than 20 euros). Despite different kinds of analytes that have been detected employing the films, a study and realization of third-generation biosensors have not yet been explored.

3.2. Direct Electron Transfer-Type Bioelectrocatalysis.

The ability of native rGO and TS-rGO films to give a DET reaction has been investigated using FDH as a model redox enzyme. To the best of our knowledge, the enzyme amount effect (in terms of activity units) on the FDH-DET reaction has not been deeply investigated, mainly because FDH-based biosensors have been developed using commercial transducers, where standardized FDH units are commonly employed.[22,37,38]

Figure 4A depicts the difference in catalytic density current (Δj, μA cm^{-2}) obtained with the whole set of rGO-films modified with FDH between 3 and 360 mU; to calculate Δj, density current at +0.4 V was recorded to take into account the whole electrocatalytic wave.[39]

Native rGO, TS-rGO$_{PET}$, and TS-rGO$_{PVC}$ showed the highest values of catalytic current density when functionalized with low amounts of enzyme (15 and 30 mU), decreasing at the smaller enzyme amount studied (3 mU). In particular, the largest and most reproducible Δj values correspond to 15 mU of FDH for these films (rGO: Δj = 185 μA cm^{-2}, RSD = 9%; TS-rGO$_{PET}$: Δj = 147 μA cm^{-2}, RSD = 1%; TS-rGO$_{PVC}$: Δj = 124 μA cm^{-2}, RSD = 6%).

This trend was different for SPE and TS-rGO$_{EVA}$ where the optimal units of the enzyme were found to be 60 mU (Δj = 46 μA cm^{-2}, RSD = 8%) and 120 mU (Δj = 54 μA cm^{-2}, RSD = 5%), respectively. Overall, SPE and TS-rGO$_{EVA}$ show smaller Δj values, highlighting the importance of the material morphology/chemistry for the catalytic process. The behavior of the SPE exhibited limited DET capacity due to the different structures of the graphitic surface. Regardless of the material studied, a notable decrease in catalytic current density was observed for the highest amounts of FDH (240 and 360 mU).

Figure 4B–F depicts the voltammetric plots obtained for all the studied films modified with 15 mU and 240 mU of FDH in the presence and absence of 10 mM D-fructose; 15 mU was selected as optimal for rGO-based films, while 240 mU is close to the enzyme amount usually employed for commercial electrodes-based biosensors.[22,38,40] No catalytic waves were recorded in nonturnover conditions (absence of D-fructose), while the measure after the addition of the substrate (turnover conditions) revealed the presence of a marked electrocatalytic wave. Except for TS-rGO$_{EVA}$, it is possible to appreciate a shoulder around 0.1 V (vs Ag/AgCl) in the anodic direction due to the electron transfer from the heme c_2 prosthetic group present in the subunit II of the FDH enzymatic structure to the electrode surface.[39,40] All the voltammograms, in agreement with Figure 4A, evidenced as in the presence of 15 mU of FDH higher catalytic currents are obtained. The extrapolated lower onset potentials (E_{onset}) confirm the higher catalytic activity at 15 mU (E_{onset}: rGO −0.081 ± 0.015 V, TS-rGO$_{PET}$ −0.106 ± 0.001 V, TS-rGO$_{PVC}$ −0.089 ± 0.001 V, TS-rGO$_{EVA}$ −0.071 ± 0.015 V, and SPE −0.068 ± 0.001 V) with respect to 240 mU (E_{onset}: rGO −0.025 ± 0.003 V, TS-rGO$_{PET}$ −0.067 ± 0.001 V, TS-rGO$_{PVC}$ −0.055 ± 0.005 V, TS-rGO$_{EVA}$ −0.033 ± 0.002 V, and SPE −0.044 ± 0.003 V). It is reasonable to speculate that since no spacers and/or cross-linkers are used to guide the enzyme immobilization, high amounts of the enzyme cause the formation of multilayers, which may (i) passivate the transducer surface reducing its electron transfer capacity and (ii) hinder the diffusion of the substrate to the active site of the enzymes in contact with the transducer.

Moreover, native-rGO is characterized by a capacitive current ∼10 fold higher than TS-rGOs: in agreement with Section 3.1, this behavior is due to 3D-film conformation and a larger amount of material. This large capacitive current does not induce a corresponding increase of catalytic current. Indeed, TS-rGO$_{PET}$ and TS-rGO$_{PVC}$ return just a slightly lower net current density. On the other hand, TS-rGO$_{PET}$ and TS-rGO$_{PVC}$ returned higher reproducibility (rGO RSD ≤ 9%, TS-rGO$_{PET}$ RSD ≤ 1%, TS-rGO$_{PVC}$ RSD ≤ 6%; n = 3). Interestingly, TS-rGOs result in a clear increase in the faradaic/capacitive current ratio during the biocatalytic direct electron transfer event.

The effect of FDH-units on the rGO-film electrochemistry was further investigated by exploring double-layer capacitance (C_S) and charge transfer resistance (R_{CT}). Figure 5A reports the

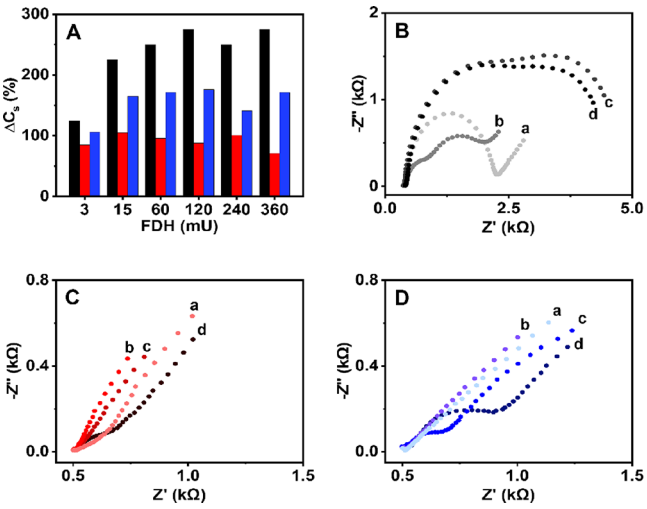

Figure 5. Double-layer capacitance and EIS were performed for SPE (black), rGO-film (red), and FDH-TS-rGO$_{PET}$ (blue) modified with different units of FDH. (A) C_S increase after film modification with different FDH units expressed as ΔC_S (%); FDH units studied are reported in the figure. (B–D) Nyquist plots obtained via EIS in 5 mM $[Fe(CN)_6]^{3-/4-}$ containing 0.1 M KCl for SPE (B), rGO-film (C) and TS-rGO$_{PET}$ (D); EIS performed on unmodified films (a), and films modified with 15 mU (b), 60 mU (c), and 240 mU (d) FDH units.

double-layer capacitance increase (ΔC_S %) with respect to the unmodified relative film in the presence of different units of FDH. This study was conducted on SPE (black bars), native rGO (red bars), and TS-rGO$_{PET}$ (blue bars). Figure S4 depicts the voltammogram comparison performed in the nonfaradaic region.

For all the studied surfaces, higher C_S values were recorded after modification with the enzyme due to a redistribution of the surface charges at the electrolyte/electrode interface caused by the protein adsorption.[41] Interestingly, the ΔC_S results are not correlated to FDH units for the native rGO. SPE and TS-rGO$_{PET}$ showed an initial increase in ΔC_S after 3 mU, reaching a plateau between 15 and 60 mU and remaining constant for higher FDH units. The ΔC_S values recorded for TS-rGO$_{PET}$ and SPE are higher than those of native rGO. In particular, SPE seems to be the most affected by the enzyme amount.

https://doi.org/10.1021/acsami.4c03339
ACS Appl. Mater. Interfaces 2024, 16, 22443−22454

Afterward, to investigate the effect of FDH adsorption on charge transfer of the redox probe, EIS was performed in the presence of $[Fe(CN)_6]^{3-/4-}$; FDH was tested at 15, 60, and 240 mU on SPE, native rGO, and TS-rGO$_{PET}$.

From the Nyquist plot of Figure 5B, the SPE exhibited a completely different behavior compared to that of rGO-based films (Figure 5C,D). In detail, the presence of an additional semicircle at lower frequencies was observed starting from the lowest quantity of FDH (15 mU); this peculiar behavior was further confirmed for 60 and 240 mU of enzyme. As stated in previous works, this Nyquist shape can be attributed to the presence of proteins (in this case FDH) blocking the electrode surface and hindering the electron transfer.[42] For this reason, EIS spectra were fitted using different equivalent circuits; the extrapolated data are expressed as the average value of three different transducers. In particular, the Randles equivalent circuit (Figure S2A) was employed to fit Nyquist plots characterized by a single semicircle, while EIS plots characterized by a double semicircle were fitted with the equivalent circuit depicted in Figure S2B; this fitting was employed for SPE-modified with FDH, for which the first semicircle obtained at higher frequencies has been attributed to the intrinsic R_{CT} of the electrode.[43] The SPE had a charge transfer resistance (R_{CT}) increase after the modification with 60 and 240 mU of FDH (R_{CT} = 2170 ± 70 Ω and R_{CT} = 2099 ± 62 Ω, respectively) with respect to pristine electrode (R_{CT} = 1754 ± 42 Ω). On the other hand, native rGO (Figure 5C) does not return significative R_{CT} changes, with only a slight increase at 240 mU of FDH (R_{CT} = 87 ± 5 Ω), whereas TS-rGO$_{PET}$ (Figure 5D) R_{CT} starts to increase at 60 mU (R_{CT} = 123 ± 7 Ω) further rising at 240 mU (R_{CT} = 302 ± 10 Ω); in both cases, a single semicircle was observed.

Overall, these data indicate how the different transducers interact differently with the FDH resulting in different electrochemically active and passive interactions. In particular, (i) the flat graphitic surface of the SPE was particularly affected by the presence of the protein, while (ii) rGO seemed to be able to accommodate high amounts of FDH with minimal influence on the electrochemical properties, most likely due to the prominent 3D porous framework. TS-rGO$_{PET}$ partially retains the native rGO features (according to Section 3.1) even with a reduced FDH loading probably due to a lower amount of material present after rGO stamping.

3.3. TS-rGO Integrated Biosensors: Analytical Performance and Application. The kinetic and analytical features of the rGO-based devices were explored through diffusion-controlled amperometry at +0.15 V. For this study, integrated sensors were employed (Section 2.2), using two different FDH amounts, i.e.,15 and 240 mU to understand the influence of the enzyme units on the electrocatalytic/analytical performance.

Figure S5 depicts the amperometric plots obtained under continuous additions of D-fructose from 1 μM to 60 mM; the extrapolated dose−response curves are depicted in Figure 6A (FDH = 15 mU) and Figure 6B (FDH = 240 mU).

All biosensors returned a Michaelis−Menten behavior[40] for both FDH amounts tested. Enzyme electrodes with 15 mU units of FDH (Figure 6A) exhibited higher currents, showing K_m^{app} values between ≈9.3 and 5.7 mM, in accordance with FDH DET-based devices reported in the literature.[38,40,44] j_{max} values were significantly higher for 15 mU compared to 240 mU, in agreement with Section 3.2. Interestingly, 15 mU FDH TS-rGO$_{PET}$ had larger j_{max} (123 ± 1 μA cm^{-2}) than native rGO (j_{max} = 93 ± 2 μA cm^{-2}). Moreover, significantly lower catalytic

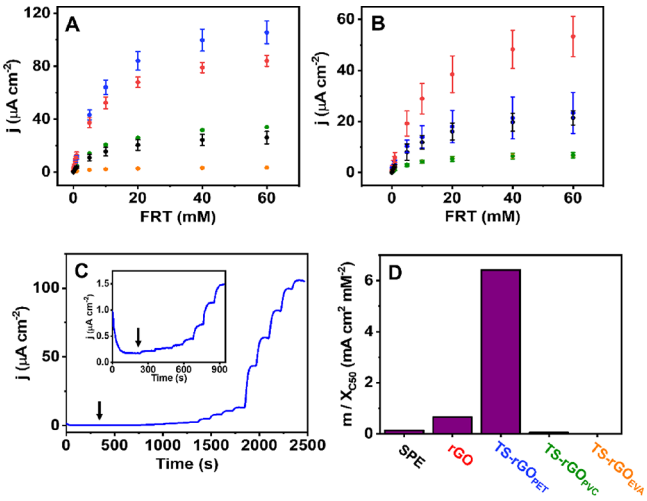

Figure 6. Amperometric measurements performed in acetate buffer under continuous additions of D-fructose (from 1 μM to 60 mM); working potential +0.15 V (vs Ag). Sensor's legend: SPE (black), rGO-film (red), TS-rGO$_{PET}$ (blue), TS-rGO$_{PVC}$ (green), TS-rGO$_{EVA}$ (orange). (A) Dose−response curves obtained with biosensors modified with 15 mU of FDH. (B) Dose−response curves obtained with biosensors modified with 240 mU of FDH. (C) Amperometric plot obtained for the FDH-TS-rGO$_{PET}$ under continuous addition of D-fructose; the inset reports the zoom of the amperometric responses for lower concentrations of D-fructose. (D) m/X_{c50} values extrapolated for the studied biosensors.

performances were recorded for TS-rGO$_{PVC}$, TS-rGO$_{EVA}$, and SPE. An opposite trend was observed employing 240 mU of FDH (Figure 6B), with native rGO showing the highest j_{max} (53 ± 1 μA cm^{-2}), significantly higher than TS-rGOs, since native rGO can accommodate a high amount of enzyme without losing electroanalytical performance. However, given the significantly lower performance obtained at 240 mU, FDH at 15 mU was employed for further studies.

Figure 6C shows the whole amperometric plot obtained with TS-rGO$_{PET}$ (FDH = 15 mU). The inset reports the data obtained for the lower D-fructose amounts. Analyzing the signals, two linear ranges were found, i.e., D-fructose of 1−10 μM (Figure S6A) and 25−250 μM (Figure S6B), respectively.

The electroanalytical features were then investigated; Table S4 lists the full set of extrapolated parameters. To compare the biosensors' figure of merits, the parameter m/X_{c50} was employed, where m represents the slope of the linear calibration curve and X_{c50} indicates the D-fructose concentration at half of the linear range. This parameter was introduced to discriminate similar sensitivities obtained with different linear ranges.[45]

Figure 6D unequivocally shows that TS-rGO$_{PET}$ possesses superior bioanalytical performance, demonstrating an m/X_{c50} ~ 10 and ~50-fold higher than native-rGO and SPE, respectively. Despite the native rGO having a similar slope, the X_{c50} (45 μM) is significantly higher given the linear range (10−100 μM). The prominent capacitive current of the native rGO (untransferred), described in Section 3.2, negatively affects the bioanalytical performance, masking the signals of the lower D-fructose amounts tested. On the other hand, FDH-TS-rGO$_{PET}$ undergoes a reduction of capacitive current thanks to thermal stamping, preserving the laser-obtained rGO-film's outstanding ability to communicate with the FDH redox site, resulting in enhanced analytical efficiency.

https://doi.org/10.1021/acsami.4c03339
ACS Appl. Mater. Interfaces 2024, 16, 22443−22454

TS-rGO$_{PET}$ superior performance is further confirmed by the obtained limit of detection (LOD), calculated using the formula $3\sigma/m$, where σ is the standard deviation of the intercept, and m is the slope of the calibration curve. TS-rGO$_{PET}$ gives rise to a LOD of 0.2 μM, significantly lower than that of the native rGO (LOD = 2.7 μM) and of other TS-RGOs (TS-rGO$_{PVC}$ LOD = 10.6 μM, TS-rGO$_{EVA}$ LOD = 11.3 μM). Compared with previous literature data, the proposed TS-rGO$_{PET}$ direct electron transfer-type biosensor demonstrates superior or at least comparable figures of merits concerning FDH-based enzymatic sensors.[40,46] In addition, the FDH-TS-rGO$_{PET}$ biosensor exhibited outstanding reproducibility, assessed considering the slope of three independent calibration curves obtained with three independent sensors (0.0289 ± 0.0008 μA cm^{-2} μM^{-1}, RSD = 3%), proving remarkable intersensor precision endorsing the robustness of the whole biosensor manufacturing process.

Eventually, to demonstrate the exploitability of FDH-TS-rGO$_{PET}$ in real applications, the biosensor has been challenged for the monitoring of D-fructose evolution during postharvest ripening of banana fruit (*Musa acuminata*). Banana ripening during storage is an irreversible process that activates biochemical and organoleptic changes,[47] including the hydrolysis of sucrose catalyzed by the enzyme invertase.[48−50] This mechanism can be modulated by atmospheric conditions[51,52] and determines significant changes from a qualitative and commercial point of view. To simulate the ripening during storage, unripe bananas belonging to the same bunch were collected and stored at room temperature, in two different environments, i.e., (i) under open air and (ii) in sealed plastic bags. The stored bananas were sampled every 2/3 days, and the D-fructose analysis was conducted according to Section 2.5; the reliability of the sensor was assessed by comparison with a commercial colorimetric enzymatic kit.

Figure 7A,B depicts examples of amperometry plots obtained at three different storage times (0th, 8th, and 17th day) for both storage conditions; Figure 7C encloses the D-fructose data obtained in comparison with the ones obtained with the commercial kit.

In agreement with the literature,[53] D-fructose levels linearly increase up to 10 days of storage in both conditions. In sealed bags, the D-fructose linear increase then plateaued instead at days 17−19. Differently, for bananas kept in air, D-fructose remains constant in days 10−12, to later rise until day 17, showing, as expected, a higher final level of D-fructose.[27]

Despite the chemical changes driven by the maturation process, the FDH-TS-rGO$_{PET}$ was able to quantify the D-fructose in a reproducible way (RSD ≤ 8%; n = 3), returning data in agreement with the colorimetric kit (relative error from −13.6% to +1.4%).

To further demonstrate the accuracy of FDH-TS-rGO$_{PET}$, recovery studies were performed for all the sampling times at three spiking levels (D-fructose 20, 40, 60 μM), obtaining satisfactory and reproducible recoveries (110−90%; RSD ≤ 7%, n = 3). Eventually, to prove the selectivity, the amperometric response of FDH-TS-rGO$_{PET}$ was studied in the presence of organic compounds, mono- and disaccharides, and ions, evaluating the D-fructose response before and after the addition of the interfering species. The obtained amperometry plot and the list of the tested compounds are reported in Figure S7. The tested compounds and their amounts have been selected according to the literature.[54] No signal perturbations were recorded, and the biosensor returned the same amperometric response obtained in buffer only. In brief, the outstanding

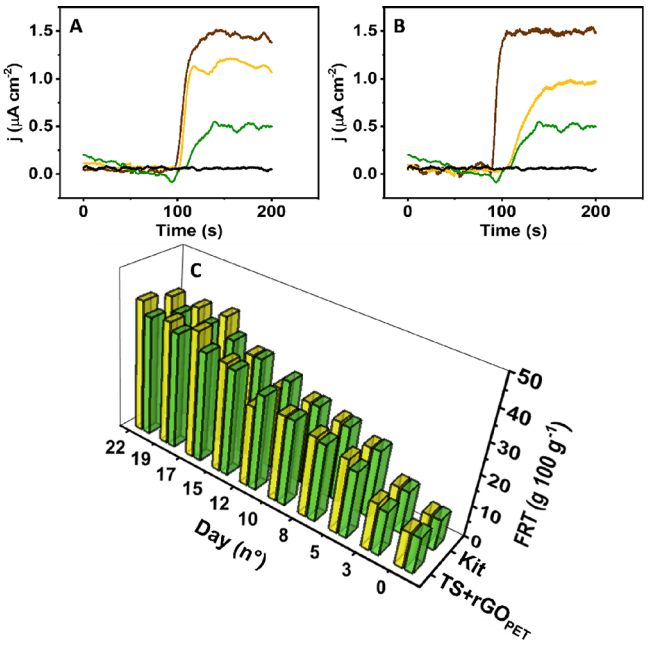

Figure 7. D-Fructose analysis in banana fruit. Amperometric curves obtained with the FDH-TS-rGO$_{PET}$, for banana sample analysis performed at different storage times, i.e., 0th (green), 8th (yellow), and 17th (brown) day; D-fructose measurement was performed on bananas stored (A) under open air and (B) in sealed plastic bags. Measurements were carried out at +0.15 V in acetate buffer. (C) D-Fructose data obtained during banana storage using the FDH-TS-rGO$_{PET}$ biosensor and the commercial enzymatic colorimetric kit; data are reported for bananas stored under open air (light yellow bars) and in sealed plastic bags (light green bars). FDH-TS-rGO$_{PET}$ data obtained for the same sample showed an RSD ≤ 7.8% (n = 3).

selectivity obtained in the presence of sugars, different from D-fructose, can be attributed to the high molecular specificity of the active site of the enzyme,[40] whereas the low working overpotential required allows us to avoid the response of potential electroactive compounds.

4. CONCLUSIONS

An easy approach has been proposed to stamp conductive laser-produced rGO films onto flexible substrates; the strategy was named roll-to-roll thermal stamping. TS-rGOs' ability to return direct electron transfer (DET) was explored in lab-made biosensors manufactured using office-grade tools.

TS-rGOs' film morphochemical and electrochemical features are dependent on the hosting substrate material chemistry and melting/transition temperatures, which play a pivotal role during thermal stamping. TS-rGOs prove the ability to undergo the DET reaction with the redox enzyme fructose dehydrogenase, showing enhanced (bio)electrocatalytic features.

TS-rGO$_{PET}$ demonstrated superior performance, thanks to its preserved rGO features and reduced capacitive current induced by the transferring process, with reproducible (RSD = 3%, n = 3) and sensitive electroanalytical features (LOD = 0.2 μM) for the determination of D-fructose. Noteworthily, TS-rGO-based biosensors allow relevant electrocatalysis using a significantly lower FDH amount (15 mU) with respect to commercial electrodes. Eventually, TS-rGO$_{PET}$ was successfully employed for the monitoring of D-fructose during banana fruit storage (Rec. 110−90%, RSD ≤ 7%; n = 3), demonstrating its applicability as a point-of-need for food control (R.E. −13/

https://doi.org/10.1021/acsami.4c03339
ACS Appl. Mater. Interfaces 2024, 16, 22443−22454

+1%), proving the potential of laser-produced transducers for third-generation biosensors.

Summing up, an easy strategy to generate controlled and effective films of laser-induced graphene onto polymeric substrates is proposed; this approach needs just a simple roll laminator and allows enhancement of the electrocatalytic features of the native material, proving great potentiality for the development of efficient on-demand (bio)electronics.

■ ASSOCIATED CONTENT

Supporting Information

The Supporting Information is available free of charge at https://pubs.acs.org/doi/10.1021/acsami.4c03339.

Figure S1: Nyquist plots of rGO-based films; Figure S2: equivalent circuits employed to fit EIS spectra; Figure S3: CV plots for double-layer capacitance extrapolation; Figure S4: CV plots for double-layer capacitance extrapolation after FDH modification; Figure S5: amperometric plots for D-fructose at increasing concentrations; Figure S6: linear relationships of D-fructose concentration and current density for FDH-TS-rGO$_{PET}$; Figure S7: study of interferents; Table S1: electrochemical parameters for $[Fe(CN)_6]^{3-/4-}$; Table S2: electrochemical parameters for $[Ru(NH_3)_6]^{3+/2+}$; Table S3: main features, electrochemical figures of merit, and applications of laser-induced graphene based on transferring strategies; Table S4: bioanalytical parameters for rGO-based biosensors (PDF)

Video S1: video of the laser-induced rGO-film roll-to-roll thermal stamping (AVI)

■ AUTHOR INFORMATION

Corresponding Authors

Flavio Della Pelle − *Department of Bioscience and Technology for Food, Agriculture and Environment, University of Teramo, Teramo 64100, Italy;* orcid.org/0000-0002-8877-7580; Email: fdellapelle@unite.it

Dario Compagnone − *Department of Bioscience and Technology for Food, Agriculture and Environment, University of Teramo, Teramo 64100, Italy;* orcid.org/0000-0001-7849-8943; Email: dcompagnone@unite.it

Authors

Davide Paolini − *Department of Bioscience and Technology for Food, Agriculture and Environment, University of Teramo, Teramo 64100, Italy*

Annalisa Scroccarello − *Department of Bioscience and Technology for Food, Agriculture and Environment, University of Teramo, Teramo 64100, Italy*

Filippo Silveri − *Department of Bioscience and Technology for Food, Agriculture and Environment, University of Teramo, Teramo 64100, Italy*

Paolo Bollella − *Department of Chemistry, University of Bari Aldo Moro, Bari 70125, Italy; Centre for Colloid and Surface Science, University of Bari Aldo Moro, Bari 70125, Italy*

Giovanni Ferraro − *Department of Chemistry "Ugo Schiff" and CSGI, University of Florence, Florence, Sesto Fiorentino 50019, Italy*

Eole Fukawa − *Division of Applied Life Sciences, Graduate School of Agriculture, Kyoto University, Kyoto 606-8502, Japan*

Yohei Suzuki − *Division of Applied Life Sciences, Graduate School of Agriculture, Kyoto University, Kyoto 606-8502, Japan*

Keisei Sowa − *Division of Applied Life Sciences, Graduate School of Agriculture, Kyoto University, Kyoto 606-8502, Japan;* orcid.org/0000-0001-9767-4922

Luisa Torsi − *Department of Chemistry, University of Bari Aldo Moro, Bari 70125, Italy; Centre for Colloid and Surface Science, University of Bari Aldo Moro, Bari 70125, Italy;* orcid.org/0000-0002-0798-0780

Complete contact information is available at: https://pubs.acs.org/10.1021/acsami.4c03339

Author Contributions

The manuscript was written through contributions of all authors. All authors have given approval to the final version of the manuscript.

Notes

The authors declare no competing financial interest.

■ ACKNOWLEDGMENTS

The authors acknowledge financial support of MUR PRIN 2022 Project No. 2022T2E7NT_01, CUP C53D23003850006, under the National Recovery and Resilience Plan (NRRP), Mission 4 Component C2 Investment 1.1—MUR call No. 104 on 2 February 2022, funded by the European Union—NextGenerationEU. G.F. acknowledge Consorzio per lo sviluppo dei Sistemi a Grande Interfase (CSGI) for financial support.

■ REFERENCES

(1) Ren, W.; Cheng, H. M. The Global Growth of Graphene. *Nat. Nanotechnol.* **2014**, *9* (10), 726−730.

(2) Luo, Y.; Shen, M.; Li, E.; Xiao, Y.; Wen, H.; Ren, Y.; Xie, J. A Chemically Modified Laser-Induced Porous Graphene Based Flexible and Ultrasensitive Electrochemical Biosensor for Sweat Glucose Detection. *Carbohydr. Polym.* **2019**, 115713.

(3) Jang, H.; Park, Y. J.; Chen, X.; Das, T.; Kim, M. S.; Ahn, J. H. Graphene-Based Flexible and Stretchable Electronics. *Adv. Mater.* **2016**, *28* (22), 4184−4202.

(4) Razaq, A.; Bibi, F.; Zheng, X.; Papadakis, R.; Jafri, S. H. M.; Li, H. Review on Graphene-, Graphene Oxide-, Reduced Graphene Oxide-Based Flexible Composites: From Fabrication to Applications. *Materials (Basel).* **2022**, *15* (3). 1012.

(5) Ares, P.; Novoselov, K. S. Recent Advances in Graphene and Other 2D Materials. *Nano Mater. Sci.* **2022**, *4* (1), 3−9.

(6) Ma, B.; Rodriguez, R. D.; Ruban, A.; Pavlov, S.; Sheremet, E. The Correlation between Electrical Conductivity and Second-Order Raman Modes of Laser-Reduced Graphene Oxide. *Phys. Chem. Chem. Phys.* **2019**, *21*, 10125−10134.

(7) Giacomelli, C.; Álvarez-Diduk, R.; Testolin, A.; Merkoçi, A. Selective Stamping of Laser Scribed RGO Nanofilms: From Sensing to Multiple Applications. *2D Mater.* **2014**, *October*, 37−41, DOI: 10.1088/2053-1583/ab68a7.

(8) Pei, S.; Cheng, H. M. The Reduction of Graphene Oxide. *Carbon N. Y.* **2012**, *50* (9), 3210−3228.

(9) Chua, C. K.; Pumera, M. Chemical Reduction of Graphene Oxide: A Synthetic Chemistry Viewpoint. *Chem. Soc. Rev.* **2014**, *43* (1), 291−312.

(10) Chilingarov, N. S.; Knot'ko, A. V.; Skokan, E. V.; Khavrel, P. A.; Levanov, A. V.; Isaikina, O. Y.; Shulga, Y. M. Microwave Exfoliated Graphite Oxide (MEGO) Heat Treatment: Transformation and Stability. *Diam. Relat. Mater.* **2021**, *120* (October), No. 108654.

(11) Jiang, C.; An, D.; Wang, Z.; Zhang, S.; An, X.; Bo, J.; Yan, G.; Moon, K. S.; Wong, C. A Sustainable Reduction Route of Graphene

Oxide by Industrial Waste Lignin for Versatile Applications in Energy and Environment. *J. Clean. Prod.* **2020**, *268*, No. 122019.
(12) Al-Hamry, A.; Kang, H.; Sowade, E.; Dzhagan, V.; Rodriguez, R. D.; Müller, C.; Zahn, D. R. T.; Baumann, R. R.; Kanoun, O. Tuning the Reduction and Conductivity of Solution-Processed Graphene Oxide by Intense Pulsed Light. *Carbon N. Y.* **2016**, *102*, 236−244.
(13) El-Kady, M.; Strong, V.; Dubin, S.; Kaner, R. Laser Scribing of High-Performance and Flexible Graphene-Based Electrochemical Capacitors. *Science (80-.).* **2012**, *335* (6074), 1326−1330.
(14) Strong, V.; Dubin, S.; El-Kady, M. F.; Lech, A.; Wang, Y.; Weiller, B. H.; Kaner, R. B. Patterning and Electronic Tuning of Laser Scribed Graphene for Flexible All-Carbon Devices. *ACS Nano* **2012**, *6* (2), 1395−1403.
(15) Kumar, R.; Joanni, E.; Singh, R. K.; da Silva, E. T. S. G.; Savu, R.; Kubota, L. T.; Moshkalev, S. A. Direct Laser Writing of Micro-Supercapacitors on Thick Graphite Oxide Films and Their Electrochemical Properties in Different Liquid Inorganic Electrolytes. *J. Colloid Interface Sci.* **2017**, *507*, 271−278.
(16) Scroccarello, A.; Álvarez-Diduk, R.; Della Pelle, F.; de Carvalho Castro e Silva, C.; Idili, A.; Parolo, C.; Compagnone, D.; Merkoçi, A. One-Step Laser Nanostructuration of Reduced Graphene Oxide Films Embedding Metal Nanoparticles for Sensing Applications. *ACS Sens.* **2023**, *8* (2), 598−609.
(17) Della Pelle, F.; Del Carlo, M.; Sergi, M.; Compagnone, D.; Escarpa, A. Press-Transferred Carbon Black Nanoparticles on Board of Microfluidic Chips for Rapid and Sensitive Amperometric Determination of Phenyl Carbamate Pesticides in Environmental Samples. *Microchim. Acta* **2016**, *183* (12), 3143−3149.
(18) Hernández-Rodríguez, J. F.; Della Pelle, F.; Rojas, D.; Compagnone, D.; Escarpa, A. Xurography-Enabled Thermally Transferred Carbon Nanomaterial-Based Electrochemical Sensors on Polyethylene Terephthalate-Ethylene Vinyl Acetate Films. *Anal. Chem.* **2020**, *92* (19), 13565−13572.
(19) Bukhari, Q. U. A.; Silveri, F.; Della Pelle, F.; Scroccarello, A.; Zappi, D.; Cozzoni, E.; Compagnone, D. Water-Phase Exfoliated Biochar Nano Fi Bers from Eucalyptus Scraps for Electrode Modi Fi Cation and Conductive Film Fabrication. *ACS Sustainable Chem. Eng.* **2021**, *9* (41), 13988−13998.
(20) Silveri, F.; Della Pelle, F.; Scroccarello, A.; Ain Bukhari, Q. U.; Del Carlo, M.; Compagnone, D. Modular Graphene Mediator Film-Based Electrochemical Pocket Device for Chlorpyrifos Determination. *Talanta* **2022**, *240*. 123212.
(21) Adachi, T.; Kitazumi, Y.; Shirai, O.; Kano, K. Direct Electron Transfer-Type Bioelectrocatalysis of Redox Enzymes at Nanostructured Electrodes. *Catalysts* **2020**, *10* (2). 236.
(22) Bollella, P.; Mazzei, F.; Favero, G.; Fusco, G.; Ludwig, R.; Gorton, L.; Antiochia, R. Improved DET Communication between Cellobiose Dehydrogenase and a Gold Electrode Modified with a Rigid Self-Assembled Monolayer and Green Metal Nanoparticles: The Role of an Ordered Nanostructuration. *Biosens. Bioelectron.* **2017**, *88* (August 2016), 196−203.
(23) Suzuki, Y.; Makino, F.; Miyata, T.; Tanaka, H.; Namba, K.; Kano, K.; Sowa, K.; Kitazumi, Y.; Shirai Suzuki, O. Y.; Sowa, K.; Kitazumi, Y.; Shirai, O.; Makino, F.; Miyata, T.; Namba, K.; Tanaka, H.; Kano, K. Structural and Bioelectrochemical Elucidation of Direct Electron Transfer-Type Membrane-Bound Fructose Dehydrogenase. *ChemRxiv* **2022**, 1−5.
(24) Chaudhary, K.; Kumar, K.; Venkatesu, P.; Masram, D. T. Protein Immobilization on Graphene Oxide or Reduced Graphene Oxide Surface and Their Applications: Influence over Activity, Structural and Thermal Stability of Protein. *Adv. Colloid Interface Sci.* **2021**, *289*, No. 102367.
(25) Kawai, S.; Goda-Tsutsumi, M.; Yakushi, T.; Kano, K.; Matsushita, K. Heterologous Overexpression and Characterization of a Flavoprotein-Cytochrome c Complex Fructose Dehydrogenase of Gluconobacter Japonicus NBRC3260. *Appl. Environ. Microbiol.* **2013**, *79* (5), 1654−1660.
(26) Fiori, S.; Scroccarello, A.; Della Pelle, F.; Del Carlo, M.; Compagnone, D. Integrated Paper/Graphene 3D Pop-up Device for the Quantitative Sensing of Carbaryl. *Sens. Actuators B Chem.* **2024**, *399* (October2023), No. 134768.
(27) Pesis, E.; Arie, R. B.; Feygenberg, O.; Villamizar, F. Ripening of Ethylene-Pretreated Bananas Is Retarded Using Modified Atmosphere and Vacuum Packaging. *HortScience* **2005**, *40* (3), 726−731.
(28) Zhao, L.; Rosati, G.; Piper, A.; de Carvalho Castro e Silva, C.; Hu, L.; Yang, Q.; Della Pelle, F.; Alvarez-Diduk, R. R.; Merkoçi, A. Laser Reduced Graphene Oxide Electrode for Pathogenic Escherichia Coli Detection. *ACS Appl. Mater. Interfaces* **2023**, *15* (7), 9024−9033.
(29) Mbayachi, V. B.; Ndayiragije, E.; Sammani, T.; Taj, S.; Mbuta, E. R.; khan, A. u. Graphene Synthesis, Characterization and Its Applications: A Review. *Results Chem.* **2021**, *3*, No. 100163.
(30) Chen, X. D.; Liu, Z. B.; Zheng, C. Y.; Xing, F.; Yan, X. Q.; Chen, Y.; Tian, J. G. High-Quality and Efficient Transfer of Large-Area Graphene Films onto Different Substrates. *Carbon N. Y.* **2013**, *56*, 271−278.
(31) Rocha, J. F.; Hostert, L.; Bejarano, M. L. M.; Cardoso, R. M.; Santos, M. D.; Maroneze, C. M.; Gongora-Rubio, M. R.; Silva, C. D. C. C. Graphene Oxide Fibers by Microfluidics Assembly: A Strategy for Structural and Dimensional Control. *Nanoscale* **2021**, *13* (14), 6752−6758.
(32) Bard, A. J.; Faulkner, L. R. Electrochemical Methods: Fundamentals and Applications. *Russ. J. Electrochem.* **2002**, *38*, 1364−1365.
(33) Lavagnini, I.; Antiochia, R.; Magno, F. An Extended Method for the Practical Evaluation of the Standard Rate Constant from Cyclic Voltammetric Data. *Electroanalysis* **2004**, *16* (6), 505−506.
(34) Della Pelle, F.; Rojas, D.; Silveri, F.; Ferraro, G.; Fratini, E.; Scroccarello, A.; Escarpa, A.; Compagnone, D. Class-Selective Voltammetric Determination of Hydroxycinnamic Acids Structural Analogs Using a WS2/Catechin-Capped AuNPs/Carbon Black−Based Nanocomposite Sensor. *Microchim. Acta* **2020**, *187* (5), 1−13.
(35) Nayak, P.; Kurra, N.; Xia, C.; Alshareef, H. N. Highly Efficient Laser Scribed Graphene Electrodes for On-Chip Electrochemical Sensing Applications. *Adv. Electron. Mater.* **2016**, *2* (10), 1−11.
(36) Voiry, D.; Chhowalla, M.; Gogotsi, Y.; Kotov, N. A.; Li, Y.; Penner, R. M.; Schaak, R. E.; Weiss, P. S. Best Practices for Reporting Electrocatalytic Performance of Nanomaterials. *ACS Nano* **2018**, *12* (10), 9635−9638.
(37) Šakinyte, I.; Barkauskas, J.; Gaidukevič, J.; Razumiene, J. Thermally Reduced Graphene Oxide: The Study and Use for Reagentless Amperometric d-Fructose Biosensors. *Talanta* **2015**, *144*, 1096−1103.
(38) Bollella, P.; Hibino, Y.; Kano, K.; Gorton, L.; Antiochia, R. Highly Sensitive Membraneless Fructose Biosensor Based on Fructose Dehydrogenase Immobilized onto Aryl Thiol Modified Highly Porous Gold Electrode: Characterization and Application in Food Samples. *Anal. Chem.* **2018**, *90* (20), 12131−12136.
(39) Bollella, P.; Boeva, Z.; Latonen, R. M.; Kano, K.; Gorton, L.; Bobacka, J. Highly Sensitive and Stable Fructose Self-Powered Biosensor Based on a Self-Charging Biosupercapacitor. *Biosens. Bioelectron.* **2021**, *176* (September 2020), No. 112909.
(40) Silveri, F.; Paolini, D.; Della Pelle, F.; Bollella, P.; Scroccarello, A.; Suzuki, Y.; Fukawa, E.; Sowa, K.; Di Franco, C.; Torsi, L.; Compagnone, D. Lab-Made Flexible Third-Generation Fructose Biosensors Based on 0D-Nanostructured Transducers. *Biosens. Bioelectron.* **2023**, *237* (June), No. 115450.
(41) Haid, R. W.; Ding, X.; Sarpey, T. K.; Bandarenka, A. S.; Garlyyev, B. Exploration of the Electrical Double-Layer Structure: Influence of Electrolyte Components on the Double-Layer Capacitance and Potential of Maximum Entropy. *Curr. Opin. Electrochem.* **2022**, *32*, No. 100882.
(42) Silveri, F.; Obořilová, R.; Máčala, J.; Compagnone, D.; Skládal, P. Impedimetric Immunosensor for Microalbuminuria Based on a WS2/Au Water-Phase Assembled Nanocomposite. *Microchim. Acta* **2023**, *190* (8), 1−12.
(43) Serafín, V.; Torrente-Rodríguez, R. M.; González-Cortés, A.; García de Frutos, P.; Sabaté, M.; Campuzano, S.; Yáñez-Sedeño, P.; Pingarrón, J. M. An Electrochemical Immunosensor for Brain

https://doi.org/10.1021/acsami.4c03339
ACS Appl. Mater. Interfaces 2024, 16, 22443−22454

Natriuretic Peptide Prepared with Screen-Printed Carbon Electrodes Nanostructured with Gold Nanoparticles Grafted through Aryl Diazonium Salt Chemistry. *Talanta* **2018**, *179* (October 2017), 131−138.
(44) Bollella, P.; Hibino, Y.; Kano, K.; Gorton, L.; Antiochia, R. The Influence of PH and Divalent/Monovalent Cations on the Internal Electron Transfer (IET), Enzymatic Activity, and Structure of Fructose Dehydrogenase. *Anal. Bioanal. Chem.* **2018**, 3253−3264.
(45) Della Pelle, F.; Vilela, D.; González, M. C.; Lo Sterzo, C.; Compagnone, D.; Del Carlo, M.; Escarpa, A. Antioxidant Capacity Index Based on Gold Nanoparticles Formation. Application to Extra Virgin Olive Oil Samples. *Food Chem.* **2015**, *178*, 70−75.
(46) Bollella, P. Enzyme-Based Amperometric Biosensors: 60 Years Later··· Quo Vadis? *Anal. Chim. Acta* **2022**, *1234*, No. 340517.
(47) Prasanna, V.; Prabha, T. N.; Tharanathan, R. N. Fruit Ripening Phenomena-an Overview. *Crit. Rev. Food Sci. Nutr.* **2007**, *47* (1), 1−19.
(48) Beaudry, R. M.; Severson, R. F.; Black, C. C.; Kays, S. J. Banana Ripening: Implications of Changes in Glycolytic Intermediate Concentrations, Glycolytic and Gluconeogenic Carbon Flux, and Fructose 2,6-Bisphosphate Concentration. *Plant Physiol.* **1989**, *91* (4), 1436−1444.
(49) Hubbard, N. L.; Pharr, D. M.; Huber, S. C. Role of Sucrose Phosphate Synthase in Sucrose Biosynthesis in Ripening Bananas and Its Relationship to the Respiratory Climacteric. *Plant Physiol.* **1990**, *94* (1), 201−208.
(50) Cordenunsi-Lysenko, B. R.; Nascimento, J. R. O.; Castro-Alves, V. C.; Purgatto, E.; Fabi, J. P.; Peroni-Okyta, F. H. G. The Starch Is (Not) Just Another Brick in the Wall: The Primary Metabolism of Sugars during Banana Ripening. *Front. Plant Sci.* **2019**, *10* (April), 452915 DOI: 10.3389/fpls.2019.00391.
(51) Phillips, K. M.; McGinty, R. C.; Couture, G.; Pehrsson, P. R.; McKillop, K.; Fukagawa, N. K.; de Brito, E. Dietary Fiber, Starch, and Sugars in Bananas at Different Stages of Ripeness in the Retail Market. *PLoS One* **2021**, *16* (7 July), No. e0253366.
(52) Özdemir, I. S. Effect of Light Treatment on the Ripening of Banana Fruit during Postharvest Handling. *Fruits* **2016**, *71* (2), 115−122.
(53) Maduwanthi, S. D. T.; Marapana, R. A. U. J. Comparative Study on Aroma Volatiles, Organic Acids, and Sugars of Ambul Banana (Musa Acuminata, AAB) Treated with Induced Ripening Agents. *J. Food Qual.* **2019**, *2019*. 1.
(54) Pickford, C.; McCormack, L.; Liu, Y.; Eicher-Miller, H. A. US Department of Agriculture Food Composition Databases, the Food and Nutrient Database for Dietary Studies 2013−2014, and the National Nutrient Database for Standard Reference Version 28 Yield Significantly Different Nutrient Totals of Food Items from Ei. *J. Acad. Nutr. Diet.* **2022**, *122* (7), 1326−1335.

https://doi.org/10.1021/acsami.4c03339
ACS Appl. Mater. Interfaces 2024, 16, 22443−22454